Article

Transverse emittance reduction in muon beams by ionization cooling

The MICE Collaboration*

Accelerated muon beams have been considered for the next-generation studies of high-energy lepton–antilepton collisions and neutrino oscillations. However, high-brightness muon beams have not yet been produced. The main challenge for muon acceleration and storage stems from the large phase-space volume occupied by the beam, derived from the production mechanism of muons through the decay of pions. The phase-space volume of the muon beam can be decreased through ionization cooling. Here we show that ionization cooling leads to a reduction in the transverse emittance of muon beams that traverse lithium hydride or liquid hydrogen absorbers in the Muon Ionization Cooling Experiment. Our results represent a substantial advance towards the realization of muon-based facilities that could operate at the energy and intensity frontiers.

Muon accelerators are considered to be potential enablers of fundamental particle physics studies at the energy and intensity frontiers. Such machines have great potential to provide multi-TeV lepton–antilepton collisions at a muon collider[1-3] or act as sources of intense neutrino beams with well-characterized fluxes and energy spectra at a neutrino factory[4-6].

The benefit of using muons in circular storage rings arises from their fundamental nature and their mass, which is 207 times that of electrons. As elementary particles, colliding muons offer the entire centre-of-mass energy to the production of short-distance reactions. This is an advantage over proton–proton colliders, such as the Large Hadron Collider[7], where each colliding proton constituent carries only a fraction of the proton energy. Compared with the electron, the larger muon mass leads to a dramatic reduction in synchrotron radiation losses, which scale as $1/m^4$. In addition, the spread in the effective centre-of-mass energy induced by beamstrahlung[8], the emission of radiation resulting from the interaction of a charged particle beam with the electric field produced by an incoming beam, is substantially lower for muons. Thus, a muon collider could achieve multi-TeV and precise centre-of-mass energies with a considerably smaller facility than an electron–positron collider such as the proposed electron–positron variant of the Future Circular Collider[9], the Circular Electron Positron Collider[10], the International Linear Collider[11] or the Compact Linear Collider[12].

The primary challenges in building a muon collider facility stem from the difficulty of producing intense muon bunches with a small phase-space volume, as well as the short muon lifetime (2.2 μs at rest). A proton-driver scheme is currently the most attractive option due to its potential to generate intense muon beams. An alternative, positron-driven muon source has been proposed and is under conceptual study[13]. In the proton-driver scheme, an intense proton beam impinges on a target to produce a secondary beam primarily composed of pions and kaons. The pions and kaons decay into muons to create a tertiary muon beam. The resulting muon beam occupies a large phase-space volume, which must be reduced (cooled) to allow efficient acceleration and sufficient flux and luminosity. The muon capture, cooling and acceleration must be executed on a timescale comparable with the muon lifetime.

Traditional cooling techniques such as stochastic cooling[14], electron cooling[15] or synchrotron radiation cooling[16] are impractical as the amount of time required to adequately cool the beam greatly exceeds the muon lifetime. Alternative muon cooling techniques are currently under development. A scheme developed at the Paul Scherrer Institute, whereby a surface muon beam is moderated to $\mathcal{O}(\mathrm{eV})$ kinetic energies in cryogenic helium gas and has its beam spot decreased using strong electric and magnetic fields, has demonstrated promising phase-space compression[17]. Another demonstrated technology is the production of ultracold muons through resonant laser ionization of muonium atoms[18]. This technique for cooling positive muons has been proposed for an $e^-\mu^+$ collider[19].

This paper describes the measurement of ionization cooling, the proposed technique by which the phase-space volume of the muon

*A list of authors and their affiliations appears at the end of the paper. ✉e-mail: paul.jurj13@imperial.ac.uk

beam can be sufficiently compressed before substantial decay losses occur[20,21]. Ionization cooling occurs when a muon beam passes through a material, known as the absorber, and loses both transverse and longitudinal momenta by ionizing atoms. The longitudinal momentum can be restored using radio-frequency accelerating cavities. The process can be repeated to achieve sufficient cooling within a suitable time frame[22].

The Muon Ionization Cooling Experiment (MICE; http://mice.iit.edu) was designed to provide the first demonstration of ionization cooling by measuring a reduction in the transverse emittance of the muon beam after the beam has passed through an absorber. A first analysis conducted by the MICE collaboration has demonstrated an unambiguous cooling signal by observing an increase in the phase-space density in the core of the beam on passage through an absorber[23]. Here we present the quantification of the ionization cooling signal by measuring the change in the beam's normalized transverse emittance, which is a central figure of merit in accelerator physics. A beam-sampling procedure is employed to improve the measurement of the cooling performance by selecting muon subsamples with optimal beam optics properties in the experimental apparatus. This beam sampling enables the probing of the cooling signal in beams with lower input emittances than those studied in the first MICE analysis[23] and facilitates a comparison between the measurement and theoretical model of ionization cooling.

Ionization cooling

The normalized root-mean-square (r.m.s.) emittance is a measure of the volume occupied by the beam in phase space. It is a commonly used quantity in accelerator physics that describes the spatial and dynamical extent of the beam, and it is a constant of motion under linear beam optics. This work focuses on the four-dimensional phase space transverse to the beam propagation axis. The MICE coordinate system is defined such that the beam travels along the z axis, and the state vector of a particle in the transverse phase space is given by $\mathbf{u} = (x, p_x, y, p_y)$. Here x and y are the position coordinates and p_x and p_y are the momentum coordinates. The normalized transverse r.m.s. emittance is defined as[24]

$$\varepsilon_\perp = \frac{1}{m_\mu c} |\mathbf{\Sigma}_\perp|^{\frac{1}{4}}, \qquad (1)$$

where m_μ is the muon mass and $|\mathbf{\Sigma}_\perp|$ is the determinant of the beam covariance matrix. The covariance matrix elements are calculated as $\mathbf{\Sigma}_{\perp,ij} = \langle u_i u_j \rangle - \langle u_i \rangle \langle u_j \rangle$.

The impact of ionization cooling on a beam crossing an absorber is best described through the rate of change of the normalized transverse r.m.s. emittance, which is approximately equal to[21,25,26]

$$\frac{d\varepsilon_\perp}{dz} \simeq -\frac{\varepsilon_\perp}{\beta^2 E_\mu} \left| \frac{dE_\mu}{dz} \right| + \frac{\beta_\perp (13.6\ \mathrm{MeV}c^{-1})^2}{2\beta^3 E_\mu m_\mu X_0}, \qquad (2)$$

where βc is the muon velocity, E_μ is the muon energy, $|dE_\mu/dz|$ is the average rate of energy loss per unit path length, X_0 is the radiation length of the absorber material and $\beta_\perp$ is the beam transverse betatron function at the absorber defined as $\beta_\perp = \frac{\langle x^2 \rangle + \langle y^2 \rangle}{2m_\mu c \varepsilon_\perp} \langle p_z \rangle$. The emittance reduction (cooling) due to ionization energy loss is expressed through the first term. The second term represents emittance growth (heating) due to multiple Coulomb scattering by the atomic nuclei, which increases the angular spread of the beam. MICE recently measured scattering in lithium hydride (LiH) and observed good agreement with the GEANT4 model[27].

The cooling is influenced by both beam properties and absorber material. Heating is weaker for beams with lower transverse betatron function at the absorber. This can be achieved by using superconducting solenoids that provide strong symmetrical focusing in the

transverse plane. The absorber material affects both terms in the equation, and optimal cooling can be realized by using materials with a low atomic number for which the product $X_0|dE_\mu/dz|$ is maximized. The performance of a cooling cell can be characterized through equilibrium emittance, which is obtained by setting $d\varepsilon_\perp/dz = 0$ and is given by

$$\varepsilon_\perp^{\mathrm{eqm}} \simeq \frac{\beta_\perp (13.6\ \mathrm{MeV}c^{-1})^2}{2\beta m_\mu X_0} \left| \frac{dE_\mu}{dz} \right|^{-1}. \qquad (3)$$

Beams having emittances below equilibrium are heated, whereas those having emittances above are cooled.

Experimental apparatus

The main component of the experiment was the MICE channel, a magnetic lattice of 12 strong-focusing superconducting coils symmetrically placed upstream and downstream of the absorber module. The schematic of the MICE channel and instrumentation is shown in Fig. 1.

Muons were produced by protons from the ISIS synchrotron[28] impinging on a titanium target[29] and were delivered to the cooling channel via a transfer line[30,31]. Tuning the fields of two bending magnets in the transfer line enabled the selection of a beam with average momentum in the range of 140–240 MeV c^{-1}. A variable-thickness brass and tungsten diffuser mounted at the entrance of the channel allowed the generation of beams with input emittance in the range of 3–10 mm.

The superconducting coils were grouped in three modules: two identical spectrometer solenoids situated upstream and downstream of the focus-coil module that housed the absorber. Each spectrometer solenoid contained three coils that provided a uniform magnetic field of up to 4 T in the tracking region, and two coils used to match the beam into or out of the focus-coil module. The focus-coil module contained a pair of coils designed to tightly focus the beam at the absorber. The large angular divergence (small $\beta_\perp$) of the focused beam reduced the emittance growth caused by multiple scattering in the absorber and increased the cooling performance. The two focus coils could be operated with identical or opposing magnetic polarities. For this study, the focus coils and the spectrometer solenoids were powered with opposite-polarity currents, thereby producing a field that flipped polarity at the centre of the absorber. This magnetic-field configuration was used to prevent the growth of the beam canonical angular momentum. The field within the tracking regions was monitored using calibrated Hall probes. A soft-iron partial return yoke was installed around the magnetic lattice to contain the field.

Due to a magnet power lead failure during the commissioning phase, one of the matching coils in the downstream spectrometer solenoid was rendered inoperable. The built-in flexibility of the magnetic lattice allowed a compromise between the cooling performance and transmission that ensured the realization of an unambiguous ionization cooling signal.

As discussed above, absorber materials with low atomic numbers are preferred for ionization cooling lattices. Lithium hydride and liquid hydrogen (LH$_2$) were the materials of choice in MICE. The LiH absorber was a disc with a thickness of 65.37 ± 0.02 mm and a density of 0.6957 ± 0.0006 g cm^{-3} (all uncertainties represent the standard error)[23]. The lithium used to produce the absorber had an isotopic composition of 95.52% ^{6}Li and 4.48% ^{7}Li.

The liquid hydrogen was contained within a 22-litre aluminium vessel: a 300-mm-diameter cylinder with a pair of dome-shaped containment windows at its ends[32]. An additional pair of aluminium windows were mounted for safety purposes. The on-axis thickness of the LH$_2$ volume was 349.6 ± 0.2 mm. The density of LH$_2$ was measured to be 0.07053 ± 0.00008 g cm^{-3} at 20.51 K (ref. 33). The cumulative on-axis thickness of the aluminium windows was 0.79 ± 0.01 mm.

A comprehensive set of detectors were used to measure the particle species, position and momentum upstream and downstream of
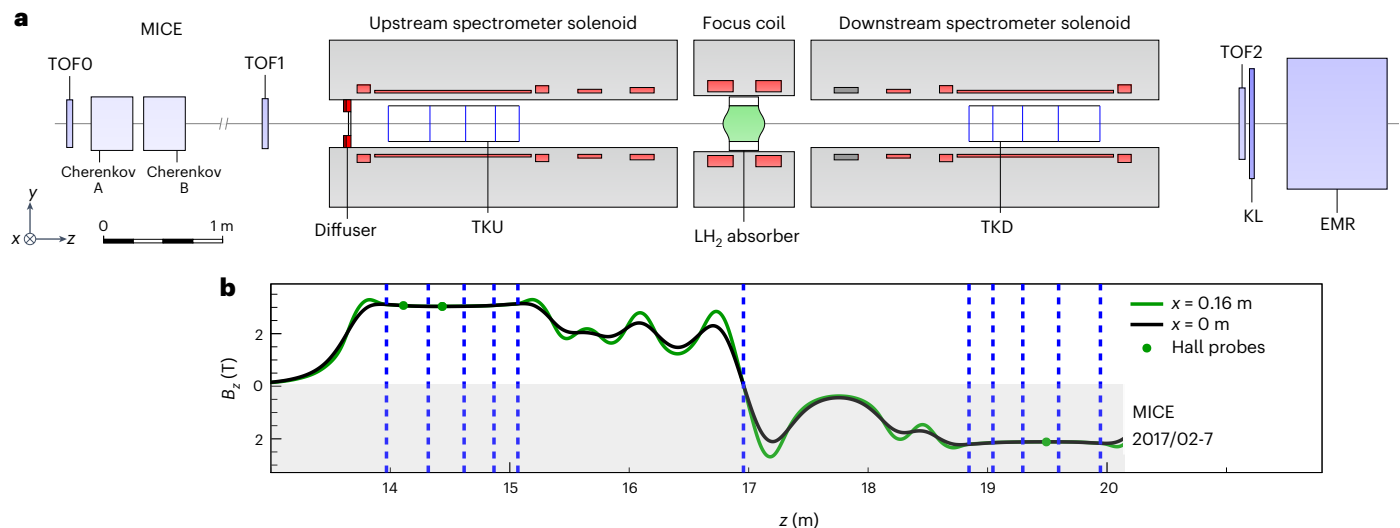
Fig. 1 | Schematic layout of the MICE experimental setup and the modelled magnetic field. a, Powered magnet coils are shown in red, absorber in green and detectors are individually labelled (see the main text for descriptions). TOF0, TOF1 and TOF2 are TOF hodoscopes; KL is a lead–scintillator pre-shower calorimeter; EMR is the electron–muon ranger. **b**, Modelled longitudinal magnetic field B_z is shown along the length of the MICE channel on axis (black line) and at 160 mm from the beam axis (green line) in the horizontal plane. The measurements of Hall probes situated at 160 mm from the axis are also shown (green circles). The vertical dashed lines indicate the positions of the tracker stations and the absorber.

the absorber[33,34]. The rate of muons delivered to the experiment was sufficiently low to allow the individual measurement of each incident particle. The data collected in cycles of several hours were aggregated offline and the phase space occupied by the beam before and after the absorber was reconstructed.

Upstream of the cooling channel, a velocity measurement provided by a pair of time-of-flight (TOF) detectors[35] was used for electron and pion rejection. A pair of threshold Cherenkov counters[36] were used to validate the TOF measurement. Downstream, a further TOF detector (TOF2)[37], a pre-shower sampling calorimeter and a fully active tracking calorimeter, namely, the electron–muon ranger[38,39], were employed to identify electrons from muon decays that occurred within the channel as well as to validate the particle measurement and identification by the upstream instrumentation. Particle position and momentum measurements upstream and downstream of the absorber were provided by two identical scintillating fibre trackers[40] immersed in the uniform magnetic fields of the spectrometer solenoids.

Each tracker (named TKU and TKD for upstream and downstream, respectively) consisted of five detector stations with a circular active area of 150 mm radius. Each station comprised three planes of 350-μm-diameter scintillating fibres, each rotated 120° with respect to its neighbour. In each station, the particle position was inferred from a coincidence of fibre signals. The particle momentum was reconstructed by fitting a helical trajectory to the reconstructed positions and accounting for multiple scattering and energy loss in the five stations[41]. For particles with a helix radius comparable with the spatial kick induced by multiple scattering, the momentum resolution was improved by combining the tracker momentum measurement with the velocity measurement provided by the upstream TOF detectors. The measurements recorded by the tracker reference planes, at the stations closest to the absorber, were used to estimate the beam emittance.

Observation of emittance reduction

The data studied here were collected using beams that passed through a lithium hydride or liquid hydrogen absorber. Scenarios with no absorber present or the empty LH$_2$ vessel were also studied for comparison. For each absorber setting, three beam-line configurations were used to deliver muon beams with nominal emittances of 4, 6 and

10 mm and a central momentum of approximately 140 MeV c^{-1} in the upstream tracker. For each beam-line/absorber configuration, the final sample contained particles that were identified as muons by the upstream TOF detectors and tracker and had one valid reconstructed trajectory in each tracker. The kinematic, fiducial and quality selection criteria for the reconstructed tracks are listed in Methods. A Monte Carlo simulation of the whole experiment was used to estimate the expected cooling performance and to study the performance of the individual detectors[42].

The beam matching into the channel slightly differed from the design beam optics due to inadequate focusing in the final section of the transfer line. This mismatch resulted in an oscillatory behaviour of the transverse betatron function in the TKU region and an increased, sub-optimal $\beta_\perp$ at the absorber, which degraded the cooling performance. An algorithm based on rejection sampling was developed to select beams with a constant betatron function in the TKU, in agreement with the design beam optics. The selection was performed on the beam ensemble measured in the TKU and was enabled by the unique MICE capability to measure the muon beams particle by particle. An example comparison between the betatron function of an unmatched parent beam and that of a matched subsample is shown in Fig. 2. The $\beta_\perp$ value of the subsample is approximately constant in the TKU, and consequently, its value at the absorber centre is ~28% smaller than the corresponding value of the parent beam.

The sampling algorithm enabled the selection of subsamples with specific emittances. This feature was exploited to study the dependence of the cooling effect on input emittance. For each absorber setting, each of the three parent beams were split into two distinct samples and six statistically independent beams with matched betatron functions ($\beta_\perp$ = 311 mm, d$\beta_\perp$/dz = 0) and emittances of 1.5, 2.5, 3.5, 4.5, 5.5 and 6.5 mm at the TKU were sampled. The numbers of muons in each sample are listed in Extended Data Table 1. The two-dimensional projections of the phase space of the sampled beams on the transverse position and momentum planes are shown in Extended Data Figs. 1 and 2, respectively.

Figure 3 shows the emittance change induced by the lithium hydride and liquid hydrogen absorbers, as well as the corresponding empty cases, for each emittance subsample. The measurement uncertainty (Fig. 3, coloured bands) is dominated by systematic
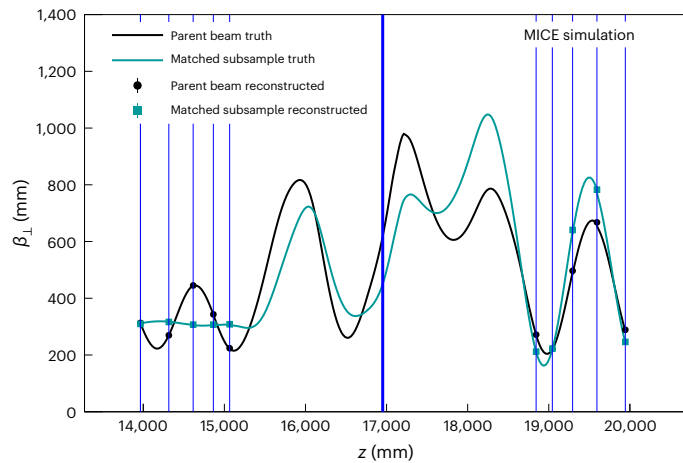
Fig. 2 | Simulated MICE muon beam betatron function. Evolution of the simulated transverse betatron function $\beta_\perp$ through the cooling channel containing the full LH_2 vessel for the parent beam (black) and matched subsample (dark cyan). The corresponding lines represent the simulation truth, whereas the circles and squares at the tracker stations (vertical blue lines) represent the reconstructed simulation. The thick vertical blue line marks the central position of the absorber. The error bars show the statistical standard error and are smaller than the markers for all the points.

uncertainties, which are listed in Extended Data Table 3 and described in detail in Methods. A correction was made to account for detector effects and for the inclusion only of events that reached the TKD. Good agreement between data and simulation is observed in all the configurations. The reconstructed data agree well with the model prediction. The model includes the heating effect in aluminium windows (Methods). The properties of the absorber and window materials used for the model calculation are listed in Extended Data Table 2.

The empty absorber cases show no cooling effects. In the empty channel case (No absorber), slight heating occurs due to optical aberrations and scattering in the aluminium windows of the two spectrometer solenoids. Additional heating caused by scattering in the windows of the LH_2 vessel is observed in the Empty LH_2 case. The LiH and Full LH_2 absorbers demonstrate emittance reduction for beams with emittances larger than ~2.5 mm. This is a clear signal of ionization cooling, a direct consequence of the presence of absorber material in the path of the beam.

For beams with 140 MeV c^{-1} momentum and $\beta_\perp$ = 450 mm at the absorber centre, the theoretical equilibrium emittances of the MICE LiH and LH_2 absorbers, including the contributions from the corresponding set of aluminium windows, are ~2.5 mm in both cases. By performing a linear fit to the measured cooling trends (Fig. 3), the effective equilibrium emittances of the absorber modules are estimated to be 2.6 ± 0.4 mm for LiH and 2.4 ± 0.4 mm for LH_2. The parameters of the linear fits to the four emittance change trends are shown in Table 1. Our null hypothesis was that for each set of six input-beam settings, the slopes of the emittance change trends in the presence and absence of an absorber are compatible. A Student's t-test found that the probabilities of observing the effects measured here are lower than 10^{-5} for both the LiH–No absorber and Full LH_2–Empty LH_2 pairs; hence, the null hypotheses were rejected.

There is no significant improvement in cooling in this measurement when using liquid hydrogen compared with lithium hydride. Scattering in the absorber windows degraded the performance of LH_2 and rendered it similar to that of LiH. MICE was based on an early stage cooling-channel concept, requiring a large-bore absorber to accommodate the beam. In lower-emittance cooling systems with smaller-bore beam pipes, the relative window thickness may be reduced, leading to a better performance of hydrogen absorbers.

Towards a muon collider

The measurement reported here demonstrates the viability of this beam cooling technique as a means of producing low-emittance muon beams for a muon collider or a neutrino factory. The muon collider targets a transverse emittance of $\mathcal{O}(10^{-2}$ mm) and a longitudinal emittance of $\mathcal{O}(10^2$ mm). To achieve these targets, substantial longitudinal and transverse emittance reduction is required, which must be demonstrated. The muon beam must traverse multiple cooling cells that produce magnetic fields stronger than those achieved by MICE and which contain high-gradient radio-frequency cavities to restore the beam longitudinal momentum[22]. Design studies for a muon cooling demonstrator facility are currently in progress[43–45].

Our measurement is an important development towards the muon cooling demonstrator, a key intermediary step in the pursuit of a muon collider. The demonstration of ionization cooling by the MICE collaboration constitutes a substantial and encouraging breakthrough in the
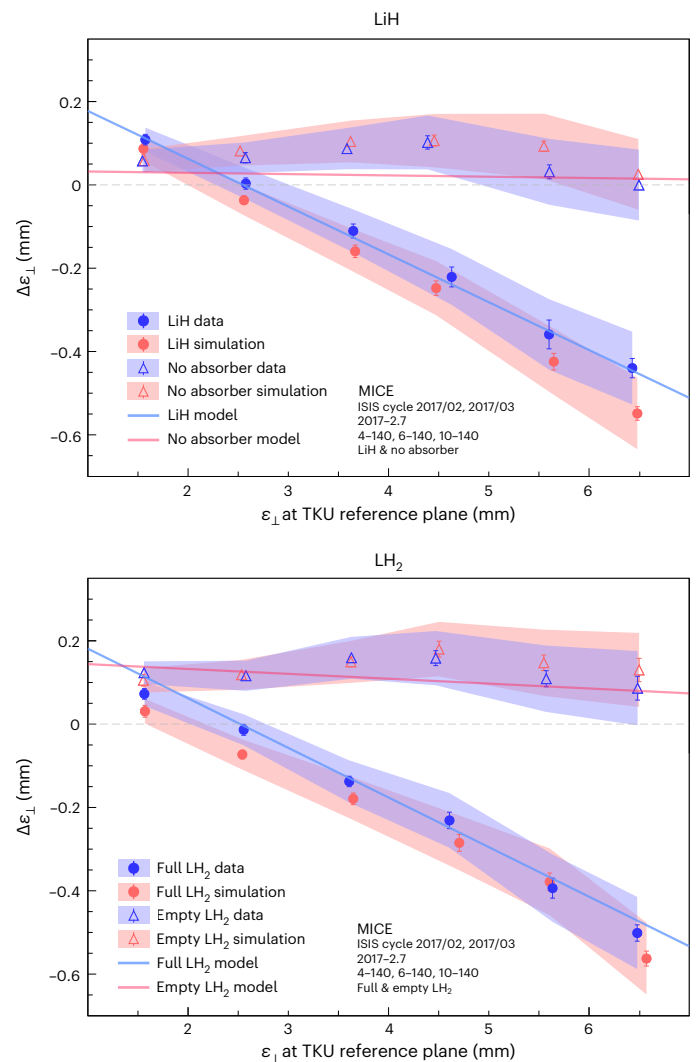

Fig. 3 | Transverse emittance change measured by MICE. Emittance change between the TKU and TKD reference planes, $\Delta\varepsilon_\perp$, as a function of emittance at TKU for 140 MeV c^{-1} beams crossing the LiH (top) and LH_2 (bottom) MICE absorbers. Results for the empty cases, namely, No absorber and Empty LH_2, are also shown. The measured effect is shown in blue, whereas the simulation is shown in red. The corresponding semitransparent bands represent the estimated total standard error. The error bars indicate the statistical error and for some of the points, they are smaller than the markers. The solid lines represent the approximate theoretical model defined by equation (10) (Methods) for the absorber (light blue) and empty (light pink) cases. The dashed grey horizontal lines indicate a scenario where no emittance change occurs.

Table 1 | Best-fit parameters of the measured emittance change trends

Absorber configuration	Intercept (mm)	Slope
No absorber	0.102±0.007	−0.011±0.012
LiH	0.297±0.006	−0.115±0.013
Empty LH$_2$	0.150±0.005	−0.006±0.013
Full LH$_2$	0.279±0.007	−0.118±0.013

Parameters of the linear fits performed on the measured emittance change trends corresponding to the four absorber configurations. Uncertainties represent the total standard error.

research and development efforts to deliver high-brightness muon beams suitable for high-intensity muon-based facilities.

Online content

Any methods, additional references, Nature Portfolio reporting summaries, source data, extended data, supplementary information, acknowledgements, peer review information; details of author contributions and competing interests; and statements of data and code availability are available at https://doi.org/10.1038/s41567-024-02547-4.

References

1. Neuffer, D. V. & Palmer, R. B. Progress toward a high-energy, high-luminosity μ⁺-μ⁻ collider. *AIP Conf. Proc.* **356**, 344–358 (1996).
2. Ankenbrandt, C. M. et al. Status of muon collider research and development and future plans. *Phys. Rev. ST Accel. Beams* **2**, 081001 (1999).
3. Palmer, R. Muon colliders. *Rev. Accel. Sci. Tech.* **7**, 137–159 (2014).
4. Geer, S. Neutrino beams from muon storage rings: characteristics and physics potential. *Phys. Rev. D* **57**, 6989–6997 (1998).
5. De Rújula, A., Gavela, M. & Hernández, P. Neutrino oscillation physics with a neutrino factory. *Nucl. Phys. B* **547**, 21–38 (1999).
6. Bogomilov, M. et al. Neutrino factory. *Phys. Rev. ST Accel. Beams* **17**, 121002 (2014).
7. Evans, L. The Large Hadron Collider. *New J. Phys.* **9**, 335 (2007).
8. Noble, R. J. Beamstrahlung from colliding electron-positron beams with negligible disruption. *Nucl. Instrum. Methods Phys. Res. A* **256**, 427–433 (1987).
9. Abada, A. et al. FCC-ee: the lepton collider. *Eur. Phys. J. Spec. Top.* **228**, 261–623 (2019).
10. CEPC Study Group et al. CEPC conceptual design report: volume 1—accelerator. Preprint at https://arxiv.org/abs/1809.00285 (2018).
11. Behnke, T. et al. The International Linear Collider technical design report—volume 1: executive summary. Preprint at https://arxiv.org/abs/1306.6327 (2013).
12. Charles, T. K. et al. The Compact Linear Collider (CLIC)—2018 summary report. Preprint at https://arxiv.org/abs/1812.06018 (2018).
13. Antonelli, M., Boscolo, M., Di Nardo, R. & Raimondi, P. Novel proposal for a low emittance muon beam using positron beam on target. *Nucl. Instrum. Methods Phys. Res. A* **807**, 101–107 (2016).
14. Möhl, D., Petrucci, G., Thorndahl, L. & Van Der Meer, S. Physics and technique of stochastic cooling. *Phys. Rep.* **58**, 73–102 (1980).
15. Parkhomchuk, V. V. & Skrinskii, A. N. Electron cooling: 35 years of development. *Phys. Uspekhi* **43**, 433–452 (2000).
16. Kolomenski, A. A. & Lebedev, A. N. The effect of radiation on the motion of relativistic electrons in a synchrotron. In *CERN Symposium on High Energy Accelerators and Pion Physics* 447–455 (CERN, 1956).
17. Antognini, A. et al. Demonstration of muon-beam transverse phase-space compression. *Phys. Rev. Lett.* **125**, 164802 (2020).
18. Bakule, P. et al. Slow muon experiment by laser resonant ionization method at RIKEN-RAL muon facility. *Spectrochim. Acta Part B* **58**, 1019–1030 (2003).
19. Hamada, Y., Kitano, R., Matsudo, R., Takaura, H. & Yoshida, M. μTRISTAN. *Prog. Theor. Exp. Phys.* **2022**, 053B02 (2022).
20. Skrinskii, A. N. & Parkhomchuk, V. V. Methods of cooling beams of charged particles. *Sov. J. Part. Nucl.* **12**, 223–247 (1981).
21. Neuffer, D. Principles and applications of muon cooling. *Part. Accel.* **14**, 75–90 (1983).
22. Stratakis, D. & Palmer, R. B. Rectilinear six-dimensional ionization cooling channel for a muon collider: a theoretical and numerical study. *Phys. Rev. ST Accel. Beams* **18**, 031003 (2015).
23. Bogomilov, M. et al. Demonstration of cooling by the muon ionization cooling experiment. *Nature* **578**, 53–59 (2020).
24. Wiedemann, H. *Particle Accelerator Physics* 4th edn (Springer Nature, 2015).
25. Penn, G. & Wurtele, J. S. Beam envelope equations for cooling of muons in solenoid fields. *Phys. Rev. Lett.* **85**, 764–767 (2000).
26. Jurj, P. B. *Normalised Transverse Emittance Reduction via Ionisation Cooling in MICE 'Flip Mode'*. PhD thesis, Imperial College London (2022).
27. Bogomilov, M. et al. Multiple Coulomb scattering of muons in lithium hydride. *Phys. Rev. D* **106**, 092003 (2022).
28. Thomason, J. The ISIS Spallation Neutron and Muon Source—the first thirty-three years. *Nucl. Instrum. Methods Phys. Res. A* **917**, 61–67 (2019).
29. Booth, C. N. et al. The design, construction and performance of the MICE target. *J. Instrum.* **8**, P03006 (2013).
30. Bogomilov, M. et al. The MICE muon beam on ISIS and the beam-line instrumentation of the Muon Ionization Cooling Experiment. *J. Instrum.* **7**, P05009 (2012).
31. Adams, D. et al. Pion contamination in the MICE muon beam. *J. Instrum.* **11**, P03001 (2016).
32. Bayliss, V. et al. The liquid-hydrogen absorber for MICE. *J. Instrum.* **13**, T09008 (2018).
33. Bogomilov, M. et al. Performance of the MICE diagnostic system. *J. Instrum.* **16**, P08046 (2021).
34. Bogomilov, M. et al. The MICE particle identification system. *Nucl. Phys. B* **215**, 316–318 (2011).
35. Bertoni, R. et al. The design and commissioning of the MICE upstream time-of-flight system. *Nucl. Instrum. Methods Phys. Res. A* **615**, 14–26 (2010).
36. Cremaldi, L., Sanders, D. A., Sonnek, P., Summers, D. J. & Reidy, J. A Cherenkov radiation detector with high density aerogels. *IEEE Trans. Nucl. Sci.* **56**, 1475–1478 (2009).
37. Bertoni, R. et al. *The Construction of the MICE TOF2 Detector* Tech. Report No. MICE-NOTE-DET-286 (MICE Collaboration, 2010).
38. Asfandiyarov, R. et al. A totally active scintillator calorimeter for the Muon Ionization Cooling Experiment (MICE). Design and construction. *Nucl. Instrum. Methods Phys. Res. A* **732**, 451–456 (2013).
39. Adams, D. et al. Electron-muon ranger: performance in the MICE muon beam. *J. Instrum.* **10**, P12012 (2015).
40. Ellis, M. et al. The design, construction and performance of the MICE scintillating fibre trackers. *Nucl. Instrum. Methods Phys. Res. A* **659**, 136–153 (2011).
41. Dobbs, A. et al. The reconstruction software for the MICE scintillating fibre trackers. *J. Instrum.* **11**, T12001 (2016).
42. Asfandiyarov, R. et al. MAUS: the MICE analysis user software. *J. Instrum.* **14**, T04005 (2019).
43. Rogers, C. A demonstrator for muon ionisation cooling. *Phys. Sci. Forum* **8**, 37 (2023).
44. Accettura, C. et al. Towards a muon collider. *Eur. Phys. J. C* **83**, 864 (2023).
45. The International Muon Collider Collaboration; https://muoncollider.web.cern.ch

The MICE Collaboration

M. Bogomilov[1], R. Tsenov[1], G. Vankova-Kirilova[1], Y. P. Song[2], J. Y. Tang[2], Z. H. Li[3], R. Bertoni[4], M. Bonesini[4], F. Chignoli[4], R. Mazza[4], A. de Bari[5], D. Orestano[6], L. Tortora[6], Y. Kuno[7], H. Sakamoto[7,33], A. Sato[7], S. Ishimoto[8], M. Chung[9], C. K. Sung[9], F. Filthaut[10,11], M. Fedorov[11], D. Jokovic[12], D. Maletic[12], M. Savic[12], N. Jovancevic[13], J. Nikolov[13], M. Vretenar[14], S. Ramberger[14], R. Asfandiyarov[15], A. Blondel[15], F. Drielsma[15,34], Y. Karadzhov[15], S. Boyd[16], J. R. Greis[16,35], T. Lord[16,36], C. Pidcott[16,37], I. Taylor[16,38], G. Charnley[17], N. Collomb[17], K. Dumbell[17], A. Gallagher[17], A. Grant[17], S. Griffiths[17], T. Hartnett[17], B. Martlew[17], A. Moss[17], A. Muir[17], I. Mullacrane[17], A. Oates[17], P. Owens[17], G. Stokes[17], P. Warburton[17], C. White[17], D. Adams[18], V. Bayliss[18], J. Boehm[18], T. W. Bradshaw[18], C. Brown[18,26], M. Courthold[18], J. Govans[18], T. Hayler[18], M. Hills[18], J. B. Lagrange[18], C. Macwaters[18], A. Nichols[18], R. Preece[18], S. Ricciardi[18], C. Rogers[18], T. Stanley[18], J. Tarrant[18], M. Tucker[18], S. Watson[18,39], A. Wilson[18], R. Bayes[19,40], J. C. Nugent[19], F. J. P. Soler[19], G. T. Chatzitheodoridis[19,20,21], A. J. Dick[20,21], K. Ronald[20,21], C. G. Whyte[20,21], A. R. Young[20,21], R. Gamet[22], P. Cooke[22], V. J. Blackmore[23], D. Colling[23], A. Dobbs[23,41], P. Dornan[23], P. Franchini[23,42], C. Hunt[23], P. B. Jurj[23] ✉, A. Kurup[23], K. Long[23], J. Martyniak[23], S. Middleton[23,43], J. Pasternak[23], M. A. Uchida[23,44], J. H. Cobb[24], C. N. Booth[25], P. Hodgson[25], J. Langlands[25], E. Overton[25,45], V. Pec[25], P. J. Smith[25], S. Wilbur[25], M. Ellis[26,46], R. B. S. Gardener[26], P. Kyberd[26], J. J. Nebrensky[26,47], A. DeMello[27], S. Gourlay[27], A. Lambert[27], D. Li[27], T. Luo[27], S. Prestemon[27], S. Virostek[27], M. Palmer[28], H. Witte[28], D. Adey[29,48], A. D. Bross[29], D. Bowring[29], A. Liu[29,49], D. Neuffer[29], M. Popovic[29], P. Rubinov[29], B. Freemire[30,49], P. Hanlet[30,50], D. M. Kaplan[30], T. A. Mohayai[30,51], D. Rajaram[30,52], P. Snopok[30], Y. Torun[30], L. M. Cremaldi[31], D. A. Sanders[31], L. R. Coney[32,53], G. G. Hanson[32] & C. Heidt[32,54]

[1]Department of Atomic Physics, St Kliment Ohridski University of Sofia, Sofia, Bulgaria. [2]Institute of High Energy Physics, Chinese Academy of Sciences, Beijing, China. [3]Sichuan University, Chengdu, China. [4]Sezione INFN Milano Bicocca, Dipartimento di Fisica G. Occhialini, Milano, Italy. [5]Sezione INFN Pavia and Dipartimento di Fisica, Università di Pavia, Pavia, Italy. [6]INFN Sezione di Roma Tre and Dipartimento di Matematica e Fisica, Università Roma Tre, Roma, Italy. [7]Department of Physics, Graduate School of Science, Osaka University, Toyonaka, Japan. [8]High Energy Accelerator Research Organization (KEK), Institute of Particle and Nuclear Studies, Tsukuba, Japan. [9]Pohang University of Science & Technology, Pohang, Korea. [10]Nikhef, Amsterdam, The Netherlands. [11]Radboud University, Nijmegen, The Netherlands. [12]Institute of Physics, University of Belgrade, Belgrade, Serbia. [13]Faculty of Sciences, University of Novi Sad, Novi Sad, Serbia. [14]CERN, Geneva, Switzerland. [15]DNPC, Section de Physique, Université de Genève, Geneva, Switzerland. [16]Department of Physics, University of Warwick, Coventry, UK. [17]STFC Daresbury Laboratory, Daresbury, UK. [18]STFC Rutherford Appleton Laboratory, Harwell Oxford, Didcot, UK. [19]School of Physics and Astronomy, University of Glasgow, Glasgow, UK. [20]SUPA and the Department of Physics, University of Strathclyde, Glasgow, UK. [21]Cockcroft Institute, Daresbury Laboratory, Daresbury, UK. [22]Department of Physics, University of Liverpool, Liverpool, UK. [23]Department of Physics, Blackett Laboratory, Imperial College London, London, UK. [24]Department of Physics, University of Oxford, Oxford, UK. [25]Department of Physics and Astronomy, University of Sheffield, Sheffield, UK. [26]College of Engineering, Design and Physical Sciences, Brunel University, Uxbridge, UK. [27]Lawrence Berkeley National Laboratory, Berkeley, CA, USA. [28]Brookhaven National Laboratory, Upton, NY, USA. [29]Fermilab, Batavia, IL, USA. [30]Illinois Institute of Technology, Chicago, IL, USA. [31]University of Mississippi, Oxford, MS, USA. [32]University of California, Riverside, CA, USA. [33]Present address: RIKEN 2-1 Horosawa, Wako, Japan. [34]Present address: SLAC National Accelerator Laboratory, Menlo Park, CA, USA. [35]Present address: TNG Technology Consulting, Unterföhring, Germany. [36]Present address: Dimensional Fund Advisors, London, UK. [37]Present address: Department of Physics and Astronomy, University of Sheffield, Sheffield, UK. [38]Present address: Defence Science and Technology Laboratory, Salisbury, UK. [39]Present address: ATC, Royal Observatory Edinburgh, Edinburgh, UK. [40]Present address: Laurentian University, Sudbury, Ontario, Canada. [41]Present address: OPERA Simulation Software, Kidlington, UK. [42]Present address: Department of Physics, Royal Holloway, University of London, Egham, UK. [43]Present address: The Division of Physics, Mathematics and Astronomy, Caltech, Pasadena, CA, USA. [44]Present address: Rutherford Building, Cavendish Laboratory, University of Cambridge, Cambridge, UK. [45]Present address: Arm, Sheffield, UK. [46]Present address: Macquarie Group, Sydney, New South Wales, Australia. [47]Present address: United Kingdom Atomic Energy Authority (UKAEA), Culham Science Centre, Abingdon, UK. [48]Present address: Institute of High Energy Physics, Chinese Academy of Sciences, Beijing, China. [49]Present address: Euclid Techlabs, Bolingbrook, IL, USA. [50]Present address: Fermilab, Batavia, IL, USA. [51]Present address: Department of Physics, Indiana University Bloomington, Bloomington, IN, USA. [52]Present address: KLA, Ann Arbor, MI, USA. [53]Present address: European Spallation Source ERIC, Lund, Sweden. [54]Present address: Swish Analytics, Oakland, CA, USA. ✉e-mail: paul.jurj13@imperial.ac.uk

Methods

Event reconstruction

Each TOF hodoscope was composed of two planes of scintillator slabs oriented along the x and y directions. Photomultiplier tubes (PMTs) at both ends of each slab were used to collect and amplify the signal produced by a charged particle traversing the slab. A coincidence of signals from the PMTs of a slab was recorded as a slab hit. A pair of orthogonal slab hits formed a space point. The information collected by the four corresponding PMTs was used to reconstruct the position and the time at which the particle passed through the detector. A detailed description of the TOF time calibration is provided elsewhere[46]. The MICE data acquisition system readout was triggered by a coincidence of signals from the PMTs of a single slab of the TOF1 detector. All the data collected by the detector system after each TOF1 trigger were aggregated, forming a particle event.

For each tracker, signals from the scintillating fibres in the five stations were combined to reconstruct the helical trajectories of the traversing charged particles. The quality of each fitted track was indicated by the χ^2 per degree of freedom as

$$\chi^2_{\mathrm{dof}} = \frac{1}{n-5} \sum_{i=1}^{n} \frac{\delta x_i^2}{\sigma_i^2}, \tag{4}$$

where n is the number of tracker planes that contributed to the reconstruction, δx_i is the distance between the measured position in the ith tracker plane and the fitted track and σ_i is the position measurement resolution in the tracker planes. A more detailed description of the reconstruction procedure and its performance can be found in other MICE work[33,41].

Sample selection

The measurements taken by the detector system were used to select the final sample. The following selection criteria ensured that a pure muon beam, with a narrow momentum spread, and fully transmitted through the channel, was selected for analysis:

- One reconstructed space point found in TOF0 and TOF1, and one reconstructed track found in TKU and TKD
- Time-of-flight between TOF0 and TOF1 consistent with that of a muon
- Momentum measured in TKU consistent with that of a muon, given the TOF0–TOF1 time-of-flight
- In each tracker, a reconstructed track contained within the cylindrical fiducial volume defined by a radius of 150 mm and with $\chi^2_{\mathrm{dof}} < 8$
- Momentum measured in TKU in the 135–145 MeV c^{-1} range
- Momentum measured in TKD in the 120–170 MeV c^{-1} range for the empty absorber configurations and 90–170 MeV c^{-1} range for the LiH and LH$_2$ absorbers
- At the diffuser, a track radial excursion contained within the diffuser aperture radius by at least 10 mm

The same set of selection criteria was applied to the simulated beams.

Beam sampling

The sampling procedure developed to obtain beams matched to the upstream tracker is based on a rejection sampling algorithm[47,48]. It was designed to carve out a beam subsample that followed a four-dimensional Gaussian distribution described by a specific (target) covariance matrix from an input-beam ensemble (parent).

The custom algorithm required an estimate of the probability density function underlying the beam ensemble. Since the MICE beams were only approximately Gaussian and approximately cylindrically symmetric, the kernel density estimation technique was used to evaluate the parent-beam density in a non-parametric fashion[49,50]. In the kernel density estimation, each data point is assigned a smooth weight

function, also known as the kernel, and the contributions from all the data points in the dataset are summed. The multivariate kernel density estimator at an arbitrary point $\mathbf{u}$ in d-dimensional space is given by

$$\hat{f}(\mathbf{u}) = \frac{1}{nh^d} \sum_{i=1}^{n} K\left(\frac{\mathbf{u} - \mathbf{u}_i}{h}\right), \tag{5}$$

where K is the kernel, n is the sample size, h is the width of the kernel and $\mathbf{u}_i$ represents the coordinate of the ith data point in the sample. In this analysis, Gaussian kernels of the following form were used:

$$K\left(\frac{\mathbf{u} - \mathbf{u}_i}{h}\right) = \frac{1}{\sqrt{(2\pi)^d |\mathbf{\Sigma}_\perp|}} \exp\left[-\frac{1}{2} \frac{(\mathbf{u} - \mathbf{u}_i)^{\mathrm{T}} \mathbf{\Sigma}_\perp^{-1} (\mathbf{u} - \mathbf{u}_i)}{h^2}\right], \tag{6}$$

where $\mathbf{\Sigma}_\perp$ is the covariance matrix of the dataset. The width of the kernel is chosen to minimize the mean integrated squared error, which measures the accuracy of the estimator[51]. Scott's rule of thumb was followed in this work, where the kernel width was determined from the sample size n and the number of dimensions d through $h = n^{-1/(d+4)}$ (ref. 50).

The kernel density estimation form described in equations (5) and (6) was used to estimate the transverse phase-space density of the initial, unmatched beams, with the estimated underlying density denoted by Parent($\mathbf{u}$). The target distribution Target($\mathbf{u}$) is a four-dimensional Gaussian defined by a covariance matrix parameterized through the transverse emittance ($\varepsilon_\perp$), transverse betatron function ($\beta_\perp$), mean longitudinal momentum and mean kinetic angular momentum[25].

The sampling was performed on the beam ensemble measured at the TKU station closest to the absorber. For each particle in the parent beam, with four-dimensional phase-space vector $\mathbf{u}_i$, the sampling algorithm worked as follows:

1. Compute the selection probability as

$$P_{\mathrm{select}}(\mathbf{u}_i) = \mathcal{C} \times \frac{\mathrm{Target}(\mathbf{u}_i)}{\mathrm{Parent}(\mathbf{u}_i)}, \tag{7}$$

where the normalization constant $\mathcal{C}$ ensures that the selection probability $P_{\mathrm{select}}(\mathbf{u}_i) \leq 1$;
2. Generate a number ξ_i from the uniform distribution $\mathcal{U}([0,1])$;
3. If $P_{\mathrm{select}}(\mathbf{u}_i) > \xi_i$, then accept the particle. Otherwise, reject it.

The normalization constant $\mathcal{C}$ was calculated before the sampling iteration presented in steps 1–3 above. It required an iteration through the parent ensemble (of size n) and it was calculated as

$$\mathcal{C} = \min_{i \in \{1, \ldots, n\}} \frac{\mathrm{Parent}(\mathbf{u}_i)}{\mathrm{Target}(\mathbf{u}_i)}. \tag{8}$$

The target parameters of interest were $\varepsilon_\perp$, $\beta_\perp$ and $\alpha_\perp = -\frac{1}{2} \mathrm{d}\beta_\perp/\mathrm{d}z$. For beams with central momentum of 140 MeV c^{-1} and a solenoidal magnetic field of 3 T, the matching conditions in the TKU were $(\beta_\perp, \alpha_\perp) = (311 \text{ mm}, 0)$. The target mean kinetic angular momentum was kept at the value measured in the parent beam for which the sampling efficiency was at a maximum.

Emittance change calculation and model

The emittance change measured by the pair of MICE scintillating fibre trackers is defined as

$$\Delta\varepsilon_\perp = \varepsilon_\perp^{\mathrm{d}} - \varepsilon_\perp^{\mathrm{u}}, \tag{9}$$

where $\varepsilon_\perp^{\mathrm{d}}$ is the emittance measured in the downstream tracker and $\varepsilon_\perp^{\mathrm{u}}$ is the emittance measured in the upstream tracker. In each tracker, the measurement is performed at the station closest to the absorber.

Starting from the cooling equation shown in equation (2), the emittance change induced by an absorber material of thickness z can be expressed as a function of the input emittance $\varepsilon_\perp^u$ as follows:

$$\Delta\varepsilon_\perp(\varepsilon_\perp^u) \approx (\varepsilon_\perp^{eqm} - \varepsilon_\perp^u)\left[1 - \exp\left(-\frac{|dE_\mu/dz|}{\beta^2 E_\mu}z\right)\right], \tag{10}$$

where $\varepsilon_\perp^{eqm}$ is the equilibrium emittance and the mean energy loss rate $|dE_\mu/dz|$ is described by the Bethe–Bloch formula[52].

The expected emittance change depends on the type and amount of material that the beam traverses between the two measurement locations. Aside from the absorber material under study and absorber-module windows, the beam crossed an additional pair of aluminium windows, one downstream of TKU and the other upstream of TKD. All the windows were made from Al 6061-T651 alloy. Equation (10) was used to estimate the theoretical cooling performance, including the effect of aluminium windows. The properties of the absorber and window materials required for the calculation are shown in Extended Data Table 2. For each absorber configuration, the beam properties required for the model (β, $\beta_\perp$, E_μ) were obtained from the simulation of the 3.5 mm beam.

Systematic uncertainties

The emittance change measurement assumes a specific arrangement of detector and magnetic fields. As this arrangement is known with limited accuracy, it is a source of systematic uncertainty in the $\Delta\varepsilon_\perp$ measurement. To assess this uncertainty, the experimental geometry was parameterized and these parameters were varied one by one in the simulation of the experiment. For each parameter considered, the resulting shift in the simulated emittance change was assigned as its associated systematic uncertainty. The following contributions to the systematic uncertainty were considered in this analysis.

Uncertainties in the tracker alignment affect the reconstructed beam phase space. A tracker displacement along an axis perpendicular to the beam line by ±3 mm and a tracker rotation about an axis perpendicular to the beam line by ±3 mrad were investigated. These variations are conservative estimates determined from the MICE tracker alignment surveys. The cylindrical symmetry of the tracker measurement was validated by performing translations and rotations along and about different axes perpendicular to the beam line.

A significant systematic uncertainty arises due to the limited knowledge of the magnetic-field strength in the tracking region, which directly impacts the momentum measurement. The three coils that produced the magnetic field in the tracking region were labelled as End 1, Centre and End 2, with the End 1 coil closest to the absorber. The effect associated with the uncertainty in the magnetic field was studied by varying the Centre coil current by ±1% and the currents in the End coils by ±5%. A conservative approach was taken when investigating the End coils, as the effect of the soft-iron partial return yoke was not included in the magnetic-field model used for track reconstruction.

The amount of energy loss and multiple scattering in each tracker station depends on the materials used. A variation of ±50% in the density of the glue used to fix the scintillating fibres was investigated. This alteration was used to account for uncertainty in the amount of silica beads added to the glue mixture.

All the sources of uncertainty presented so far were studied in both spectrometer solenoids. Additionally, as the TOF01 time measurement was used to assist the momentum reconstruction of muons with low transverse momentum, a variation corresponding to the 60 ps uncertainty on the TOF measurement was studied. The uncertainties associated with the individual parameter alterations are shown in Extended Data Table 3, for beams with input emittances in the [1.5, 2.5...6.5] mm range. For each input emittance, the total systematic uncertainty was obtained by adding all the individual contributions in quadrature.

Data availability

Code availability

References

46. Karadzhov, Y., Bonesini, M., Graulich, J. S. & Tzenov, R. *TOF Detectors Time Calibration* Tech. Report No. 251 (2009).
47. von Neumann, J. Various techniques used in connection with random digits. *J. Res. Natl Bureau Stand. Appl. Math. Series* **12**, 36–38 (1951).
48. Wells, M. T., Casella, G. & Robert, C. P. Generalized accept-reject sampling schemes. *Lect. Notes Monogr. Series* **45**, 342–348 (2004).
49. Silverman, B. W. *Density Estimation for Statistics and Data Analysis* 1st edn (Routledge, 1998).
50. Scott, D. W. *Multivariate Density Estimation: Theory, Practice, and Visualization* (John Wiley & Sons, 2015).
51. Marron, J. S. & Wand, M. P. Exact mean integrated squared error. *Ann. Stat.* **20**, 712–736 (1992).
52. Leroy, C. & Rancoita, P. G. *Principles of Radiation Interaction in Matter and Detection* (World Scientific, 2011).
53. Bogomilov, M. et al. MICE raw data. *figshare* https://doi.org/10.17633/rd.brunel.3179644.v1 (2016).
54. Bogomilov, M. et al. MICE reconstructed data. *figshare* https://doi.org/10.17633/rd.brunel.5955850.v1 (2018).
55. Bogomilov, M. et al. Source code of MAUS—the MICE analysis user software. *figshare* https://doi.org/10.17633/rd.brunel.8337542.v2 (2019).
56. Zyla, P. A. et al. Review of particle physics. *Progr. Theor. Exp. Phys.* **2020**, 083C01 (2020).

Acknowledgements

Author contributions

All authors contributed considerably to the design or construction of the apparatus or to the data taking or analysis described in this Article.

Competing interests

The authors declare no competing interests.

Additional information

Extended data is available for this paper at https://doi.org/10.1038/s41567-024-02547-4.

Supplementary information The online version contains supplementary material available at https://doi.org/10.1038/s41567-024-02547-4.

**Correspondence and requests for materials** should be addressed to P. B. Jurj.

Peer review information *Nature Physics* thanks Seweryn Kowalski and Masashi Otani for their contribution to the peer review of this work.

Reprints and permissions information is available at www.nature.com/reprints.
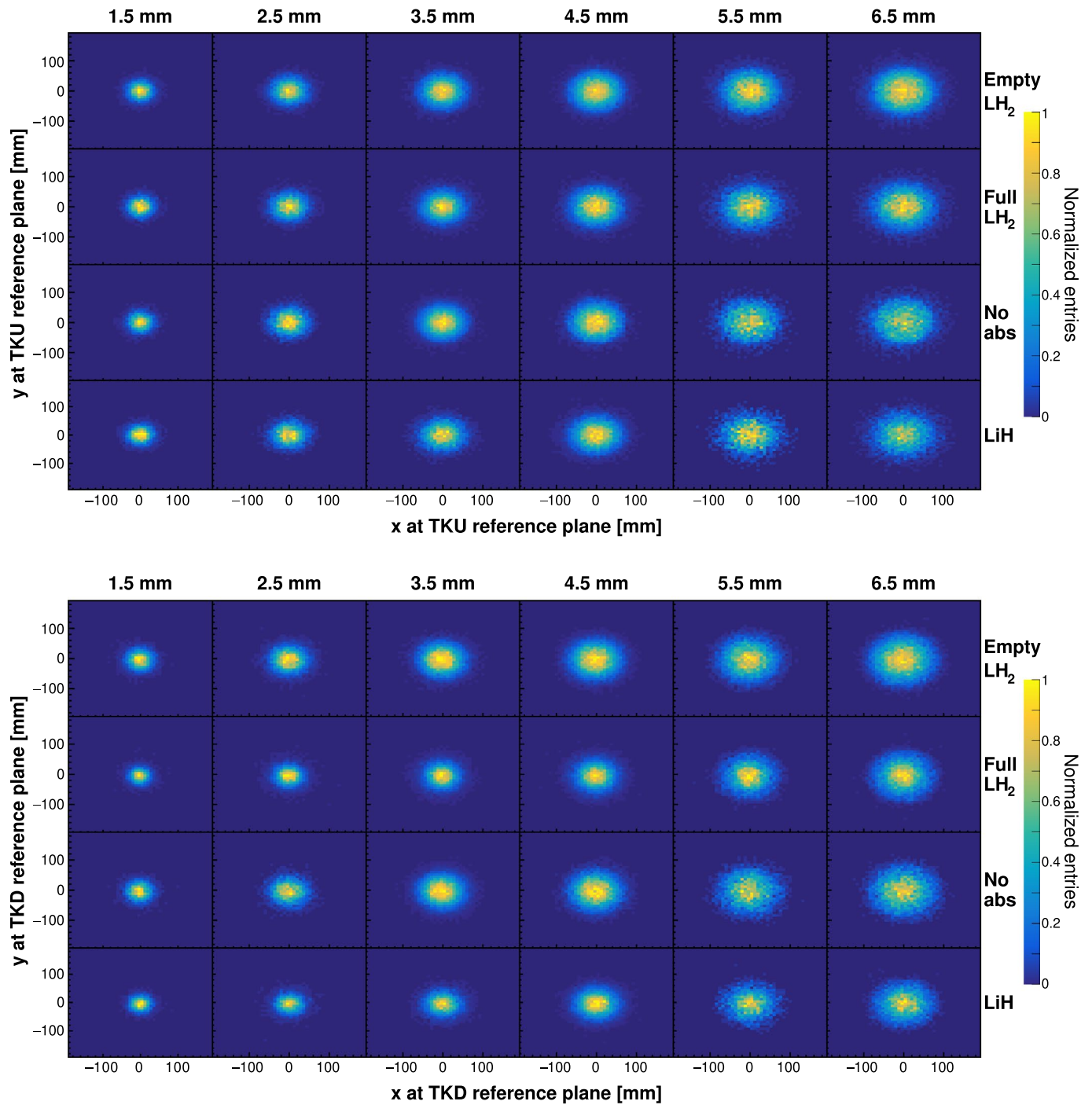
Extended Data Fig. 1 | Beam transverse profiles in the (top) upstream and (bottom) downstream trackers (TKU and TKD). Measured transverse beam profiles for each absorber configuration (rows) and input emittance (columns). In each histogram, the number of events in each bin is normalized to the number of events contained by the bin with most entries. The beams that pass through an absorber present a smaller transverse size in the downstream tracker than the beams that traverse an empty absorber module. This effect is caused by a change in focusing due to energy loss.
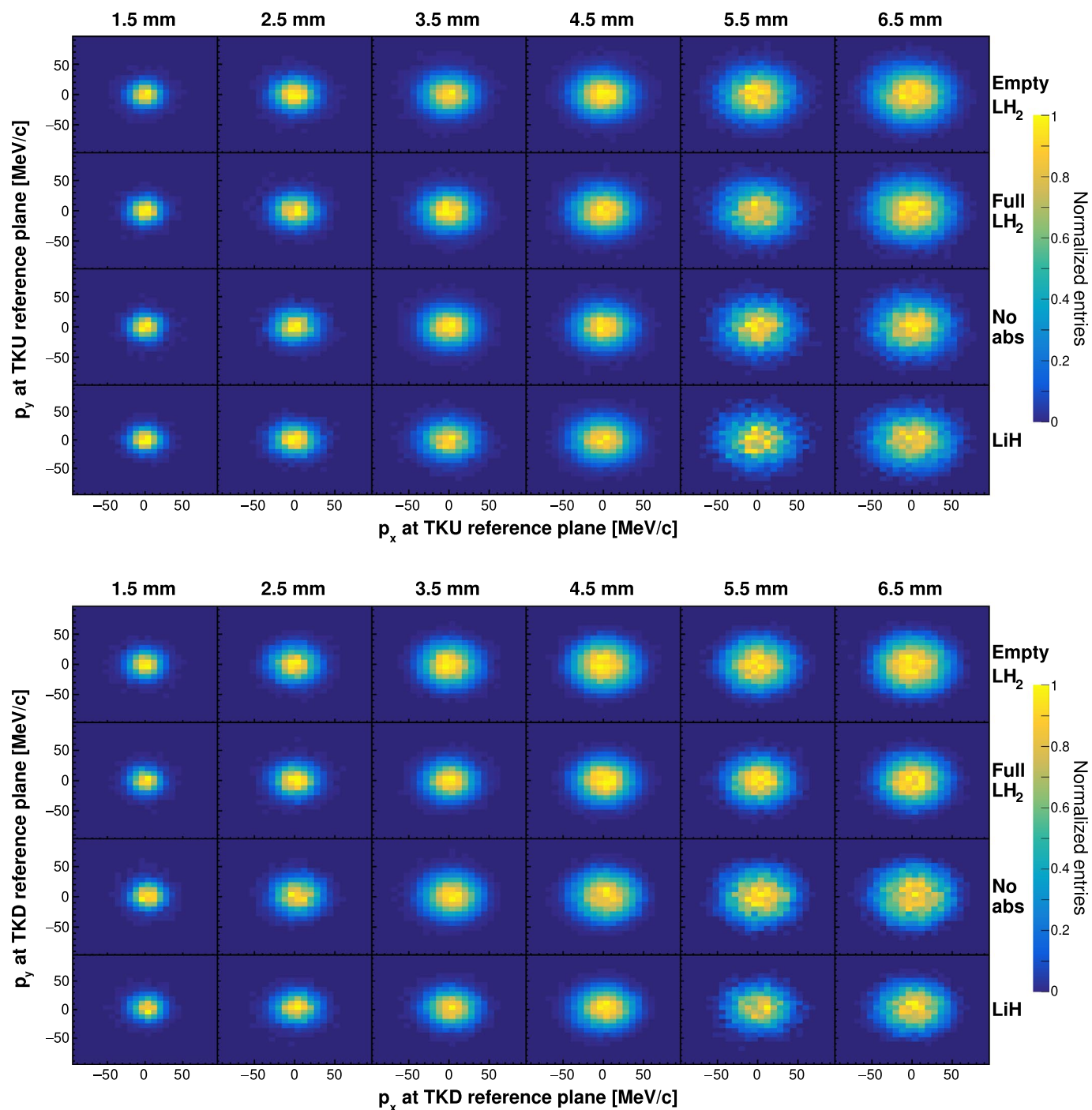
Extended Data Fig. 2 | Beam transverse momentum in the (top) upstream and (bottom) downstream trackers (TKU and TKD). Measured x and y components of the beam transverse momentum, p_x and p_y, for each absorber configuration (rows) and input emittance (columns). In each histogram, the number of events in each bin is normalized to the number of events contained by the bin with most entries. The beams that pass through an absorber present a smaller transverse momentum in the downstream tracker than the beams that traverse an empty absorber module.

Extended Data Table 1 | The sample size of the MICE matched beams

Absorber	Input $\varepsilon_\perp$ [mm] 1.5	2.5	3.5	4.5	5.5	6.5
Empty LH$_2$	8141	10162	19525	29896	13196	22080
Full LH$_2$	5199	8541	16757	20836	9063	15326
No absorber	4496	4792	32836	17659	5324	8573
LiH	4549	4372	9150	21071	3927	7618

The number of muons in each final sample is listed for each absorber configuration and target input transverse emittance $\varepsilon_\perp$.

Extended Data Table 2 | Material properties of the MICE absorbers and aluminium alloy windows

Property ╲ Material	MICE LiH	Liquid H_2	Al 6061-T651
Density, ρ [g/cm^3]	0.6957	0.07053	2.727
$\langle Z/A \rangle$	0.56716	0.99212	0.48145
I [eV]	36.5	21.8	166
X_0 [cm]	102.04	866	8.68

Z and A are the atomic and mass numbers of the material, respectively, I is the mean excitation energy of the atoms in the material, and X_0 is the radiation length of the material[56].

Extended Data Table 3 | Systematic uncertainties affecting the measurement of emittance change Δ$\varepsilon_\perp$

Parameter alteration \ Input $\varepsilon_\perp$ [mm]	Systematic uncertainty [mm]					
	1.5	2.5	3.5	4.5	5.5	6.5
TKU translation	0.003	0.002	0.001	0.005	0.003	0.002
TKU rotation	0.003	0.003	0.002	0.005	< 0.001	0.003
TKU glue density	0.003	0.001	0.003	0.003	0.004	0.002
Upstream End 1 coil current	0.009	0.011	0.016	0.018	0.024	0.023
Upstream Centre coil current	0.018	0.021	0.028	0.034	0.042	0.050
Upstream End 2 coil current	0.007	0.006	0.006	0.005	0.010	0.015
TKD translation	0.003	0.003	0.001	0.001	0.004	< 0.001
TKD rotation	0.001	0.002	0.001	0.005	< 0.001	0.001
TKD glue density	0.005	< 0.001	0.001	0.004	0.003	0.002
Downstream End 1 coil current	0.003	0.010	0.014	0.018	0.024	0.027
Downstream Centre coil current	0.013	0.021	0.032	0.044	0.053	0.054
Downstream End 2 coil current	0.001	0.005	0.009	0.007	0.008	0.012
TOF01 time	0.001	< 0.001	0.004	0.006	0.007	0.007
Total systematic uncertainty	0.026	0.035	0.048	0.063	0.077	0.084

The systematic uncertainties associated with parameter alterations in the upstream tracker (TKU), downstream tracker (TKD), upstream and downstream coils, and time-of-flight measurement (TOF01) are listed for each input transverse emittance $\varepsilon_\perp$.